

Ultrafast transverse and longitudinal response of laser-excited quantum wires

JEREMY R. GULLEY^{1,*} AND DANHONG HUANG²

¹*Department of Physics, Kennesaw State University, Kennesaw, GA 30144, USA*

²*Air Force Research Laboratory, Space Vehicles Directorate (AFRL/RVS), Kirtland Air Force Base, New Mexico 87117, USA*

*jgulley@kennesaw.edu

Abstract: We couple 1D pulse propagation simulations with laser-solid dynamics in a GaAs quantum wire, solving for the electron and hole populations and the interband and intraband coherences between states. We thus model not only the dynamical dipole contributions to the optical polarization (interband bound-charge response) but also the photo-generation and back-action effects of the net free-charge density (intraband free-charge response). These results show that solving for the dynamic electron and hole intraband coherences leads to plasma oscillations at THz frequencies, even in a 1D solid where plasma screening is small. We then calculate the transverse and longitudinal response of the quantum wire and characterize the dispersion relation for the e - h plasma. This approach allows one to predict the optoelectronic response of 1D semiconductor devices during and after exposure to resonant ultrashort pulses.

© 2022 Optica Publishing Group under the terms of the [Optica Open Access Publishing Agreement](#)

1. Introduction

The behavior of electron-hole plasmas in a nanometer-scale solid does not follow the classical laws of electronics. Instead, it obeys the laws of quantum physics and Fermi-Dirac statistics [1]. The entire research field of optoelectronics is concerned with explaining the quantum interaction of electronic material components with light, increasingly on the nanometer-scale. The transport properties of these light-generated plasmas are hard to predict on time scales of femtoseconds or attoseconds, since most thermal and other relaxation effects require picoseconds or longer to drive the plasma to a quasi-equilibrium state [2]. This predictive ability is critical for many current research topics such as terahertz generation and detection [3–6], remote sensing [3,7], high-harmonic generation and atto-second physics [8–15], high field optoelectronics [9,10,16], photovoltaics [17,18] as well as nanoplasmonics [19–21]. Although the strong interaction of photons with electrons in a solid is ultrashort in time duration, photons still leave their fingerprints on excited electron-hole pairs. The dynamics of excited pairs can be detected through a delayed light pulse as a stored photon memory [22] from the pump pulse. In the perturbation regime, where the laser field is much less than the fields within the atom, the nonlinear optical response of incident light can be studied, such as the Kerr effect and sum-frequency generation [23,24]. However, for higher field strengths used in optical writing [25,26] and memory [22], these ultrafast processes are not fully described by a perturbation model.

Laser-generated e - h plasmas in semiconductors are different from gaseous plasmas because, at low temperatures, they are dense, ordered, and confined. Only after valence band electrons are excited into conducting states do the interacting electrons (and the holes they leave behind) behave as a plasma in an undoped semiconductor [27]. Optically generating a plasma in semiconductors using ultrashort laser pulses requires light intensities on the order of a GW/cm^2 , ensuring that the laser-plasma interactions are nonlinear [28]. To thoroughly understand the physics of laser-induced e - h plasmas, one must model the change in the propagation of the laser field while it interacts with the solid. Specifically, self-consistently solving the Maxwell equations requires both transverse and longitudinal fields, as well as source terms; charge densities, current

densities, and polarizations. In this way, the induced fields from excited plasmas act back on photo-generated e - h pairs, i.e. high-order correlation effect.

Recently, a self-consistent quantum-kinetic model for both optical e - h plasma generation, plasma transport, and pulse propagation was developed within a single framework [29]. This model is ideal for laser interaction with nanowires because the quantum excitation and transport is confined along a single dimension in space, thus simplifying the calculations. In this model, the interactions of quantum-wire electrons with both propagating transverse and localized longitudinal electric fields are included. Also included is the back action of optical polarizations and net plasma free-charge density on transverse and longitudinal electric fields. In this work we modify the model in [29] to include the dynamical intraband electron and hole coherences (free-charge plasma response) in addition to the traditional intraband coherences (bound-charge polarization response). Our results show that solving for the dynamic electron and hole intraband coherences leads to plasma oscillations at THz frequencies, even in a 1D solid where plasma screening is small [27]. We use these results to characterize the dielectric and optoelectronic response of a two-band GaAs quantum wire to resonant ultrafast light, where the photon energy approximately equals the band gap. Due to the 1D nature of both the quantum wire and the propagation space, the transverse (optical) and longitudinal (plasmonic) fields and dielectric responses are easily distinguished. We compare numerical results for the dielectric response from this model to analytical predictions within the random phase approximation after the e - h plasma has reached a quasi-equilibrium.

2. Theory and numerical methods

2.1. Field propagation equations

Figure 1 gives a schematic for this work. The 1D laser field propagates in the y -direction with the transverse electric field $E_x^\perp(y, t)$ linearly polarized along the x -direction and the magnetic field $H_z^\perp(y, t)$ along the z -direction. During and after resonant excitation of the quantum wire, the e - h plasma forms a net free-charge density in the wire, giving rise to a longitudinal electric field $E_y^\parallel(y, t)$ along the y -direction. In this work we assume all materials are nonmagnetic, so there is no longitudinal magnetic field $H_z^\parallel(y, t)$. We solve for the fields using Pseudo-Spectral Time Domain (PSTD) methods [30] in which the 1D Maxwell equations are:

$$\partial_t \tilde{H}_z^\perp(q, t) = -iq \tilde{E}_x^\perp(q, t) \mu_0^{-1}, \quad (1a)$$

$$\partial_t \tilde{D}_x^\perp(q, t) = -iq \tilde{H}_z^\perp(q, t), \quad (1b)$$

$$\partial_t \tilde{D}_y^\parallel(q, t) = -\tilde{J}_y^\parallel(q, t), \quad (1c)$$

$$-iq \tilde{D}_y^\parallel(q, t) = \tilde{\rho}_f(q, t), \quad (1d)$$

where the tilde indicates spatial Fourier transform, q is the wavenumber along the y -direction, and $\tilde{D}_{x,y}^{\perp,\parallel}$ is the electric displacement such that $\tilde{D}_{x,y}^{\perp,\parallel} = \epsilon_b \epsilon_0 \tilde{E}_{x,y}^{\perp,\parallel} + \tilde{P}_{x,y}^{\perp,\parallel}$. Here, $\tilde{P}_{x,y}^{\perp,\parallel}(q, t)$ is the induced polarization of the quantum wire and ϵ_b is the background dielectric constant from the AlAs host. Equations (1c) and (1d) are redundant, and since our model for the quantum wire naturally calculates $\tilde{\rho}_f(q, t)$, Eq. (1c) is not needed.

Therefore, at each time-step, the transverse and longitudinal electric fields are given by:

$$\tilde{E}_x^\perp(q, t) = \frac{\tilde{D}_x^\perp(q, t)}{\epsilon_0 \epsilon_b} - \frac{\tilde{P}_x^\perp(q, t)}{\epsilon_0 \epsilon_b}, \quad (2a)$$

$$\tilde{E}_y^\parallel(q, t) = \frac{-\tilde{\rho}_f(q, t)}{iq \epsilon_0 \epsilon_b} - \frac{\tilde{P}_y^\parallel(q, t)}{\epsilon_0 \epsilon_b}. \quad (2b)$$

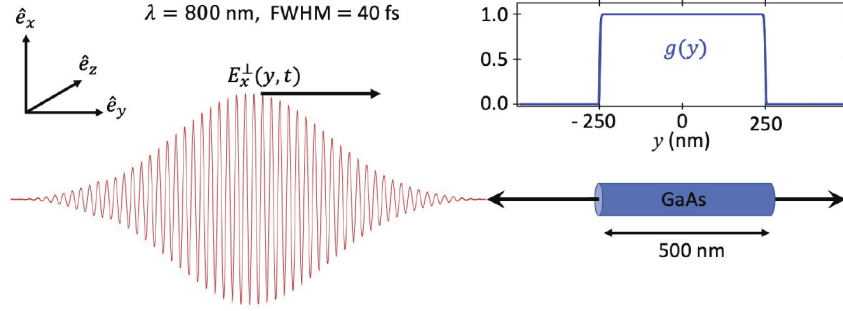


Fig. 1. Schematic of the simulation. The laser pulse field $E_x^\perp(y, t)$ (shown in red) propagates in the y -direction down the axis of a 500 nm long GaAs quantum wire. The quantum wire gating function $g(y)$ is plotted in the inset.

2.2. Bound charge response

Although the Maxwell equations are solved in the q -space, the propagation simulations also record $E_{x,y}^{\perp,\parallel}(y, t)$ for all y and t . The Maxwell fields that enter the quantum wire Hamiltonian are gated by the wavefunction envelope which we take to be a normalized super-Gaussian of order N , $g(y) = \exp[-(2y/\mathcal{L})^N]/\Gamma[N/(N-1)]$, where \mathcal{L} is the length of the quantum wire and the value of $g(y)$ is approximately zero outside the wire and ~ 1 inside the wire ($|y| \leq \mathcal{L}/2$). For our simulations, $N = 150$ provides a soft boundary of ± 5 nm about the wire edges (ideal for numerical Fourier transforms). This gate function is plotted in the inset of Fig. 1. We then define the gated electric field inside the wire as

$$\mathcal{E}_{x,y}^{\perp,\parallel}(y, t) = E_{x,y}^{\perp,\parallel}(y, t) g(y), \quad (3)$$

and express the q -space Fourier transform of this quantity as

$$\tilde{\mathbf{E}}(q, t) = \tilde{\mathcal{E}}_x^\perp(q, t) \hat{\mathbf{e}}_x + \tilde{\mathcal{E}}_y^\parallel(q, t) \hat{\mathbf{e}}_y. \quad (4)$$

The corresponding polarization components $\tilde{P}_{x,y}^{\perp,\parallel}(q, t)$ are calculated from the solutions to the two-band Semiconductor Bloch Equations (SBEs) as described in Ref. [29]. Our use of only two bands is justified by our pumping the quantum wire at resonance. The SBEs time-evolve electron and hole occupation numbers at momentum k , $n_k^e(t)$ and $n_k^h(t)$, and the coherence between electrons at momentum k and holes at momentum k' , $\mathbf{p}_{k,k'}(t)$, yielding

$$\frac{dn_k^e(t)}{dt} = \frac{2}{\hbar} \sum_{k'} \text{Im} \{ \mathbf{p}_{k,k'}(t) \cdot \mathbf{\Omega}_{k',k}(t) \} + \left. \frac{\partial n_k^e(t)}{\partial t} \right|_{\text{rel}}, \quad (5a)$$

$$\frac{dn_{k'}^h(t)}{dt} = \frac{2}{\hbar} \sum_k \text{Im} \{ \mathbf{p}_{k,k'}(t) \cdot \mathbf{\Omega}_{k',k}(t) \} + \left. \frac{\partial n_{k'}^h(t)}{\partial t} \right|_{\text{rel}}, \quad (5b)$$

$$\begin{aligned} i\hbar \frac{d\mathbf{p}_{k,k'}(t)}{dt} &= [\varepsilon_k^e + \varepsilon_{k'}^h + \varepsilon_G + \Delta\varepsilon_k^e + \Delta\varepsilon_{k'}^h - i\hbar\Gamma_k^e - i\hbar\Gamma_{k'}^h] \mathbf{p}_{k,k'}(t) \\ &\quad - [1 - n_k^e(t) - n_{k'}^h(t)] \hbar\mathbf{\Omega}_{k,k'}(t) \\ &\quad + i\hbar \sum_{q \neq 0} \Lambda_{k,q}^e(t) \mathbf{p}_{k+q,k'}(t) + i\hbar \sum_{q' \neq 0} \Lambda_{k',q'}^h(t) \mathbf{p}_{k,k'+q'}(t), \end{aligned} \quad (5c)$$

where $\mathbf{p}_{k,k'}(t) = \sum_{j=x,y} p_{k,k'}^j(t) \hat{\mathbf{e}}_j$ is the microscopic polarization, $\hat{\mathbf{e}}_j$ represent the unit vectors in the x and y directions, and the spin degeneracy of carriers is included. For a wire with periodic

boundary conditions, the macroscopic quantum wire polarization is given by

$$\tilde{\mathbf{P}}(q, t) = \frac{\alpha}{2\delta_0\mathcal{L}} \sum_k d_{cv} \mathbf{p}_{k+q,k}(t) + \text{c.c.},$$

where $1/\alpha$ is an effective quantum wire thickness in the x -direction, and δ_0 is the wire thickness in the z -direction, the dipole-coupling matrix element at the Γ point is calculated as $d_{cv} = \sqrt{(3e^2\hbar^2/4m_0\varepsilon_G)[(m_0/m_e^*) - 1]}$ [31,32], and m_0 is the free-electron mass. However, to account for the borders of the quantum wire as given by the wire envelope function $g(y)$, we calculate the polarization in the y -space of the wire as

$$\mathbf{P}(y, t) = \frac{\alpha}{2\delta_0\mathcal{L}} \sum_{k,k'} d_{cv} \mathbf{p}_{k,k'}(t) e^{i(k'-k)y} g(y) + \text{c.c.}, \quad (6)$$

where this polarization can be divided into transverse and longitudinal components in like manner to Eq. (4),

$$\mathbf{P}(y, t) = \mathbf{P}_x^\perp(y, t) \hat{\mathbf{e}}_x + \mathbf{P}_y^\parallel(y, t) \hat{\mathbf{e}}_y. \quad (7)$$

In Eq. (5c), the energy ε_G is the bandgap of the quantum wire, $\varepsilon_k^{e,h} = \hbar^2 k^2 / 2m_{e,h}^*$ are the electron and hole single-particle energies, $m_{e,h}^*$ are the electron and hole effective masses, and $\Delta\varepsilon_k^e$ and $\Delta\varepsilon_k^h$ are the Coulomb renormalization of these energies given by [7]:

$$\Delta\varepsilon_k^e = 2 \sum_q n_q^e(t) V_{k,q;q,k}^{ee} - \sum_{q \neq k} n_q^e(t) V_{k,q;k,q}^{ee} - 2 \sum_{q'} n_{q'}^h(t) V_{k,q';q',k}^{eh}, \quad (8a)$$

$$\Delta\varepsilon_k^h = 2 \sum_{q'} n_{q'}^h(t) V_{k',q';q',k'}^{hh} - \sum_{q' \neq k'} n_{q'}^h(t) V_{k',q';k',q'}^{hh} - 2 \sum_q n_q^e(t) V_{q,k';k',q}^{eh}, \quad (8b)$$

The quantities $\Gamma_{j,k}^e(t)$ and $\Gamma_{j,k'}^h(t)$ are the electron and hole diagonal dephasing rates while $\Lambda_{j,k,q}^e(t)$ and $\Lambda_{j,k',q'}^h(t)$ are the off-diagonal dephasing rates as detailed in the Appendix of Ref. [29]. The last term in Eqs. (5a) and (5b) are scattering terms containing carrier-phonon scattering and Coulomb scattering. They are calculated by $\partial_t n_k^{e,h} |_{\text{rel}} = W_{k,(\text{in})}^{e,h} (1 - n_k^{e,h}) - W_{k,(\text{out})}^{e,h} n_k^{e,h}$, where the in and out scattering rates, $W_{k,(\text{in})}^{e,h}$ and $W_{k,(\text{out})}^{e,h}$, are also given in the Appendix of Ref. [29].

The renormalized Rabi frequency $\Omega_{k,k'}(t)$ in Eqs. (5a)–(5c) for a 1D space is

$$\Omega_{k,k'}(t) = \frac{d_{cv}}{\hbar} \tilde{\mathbf{E}}(k - k', t) + \sum_{k_1 \neq k, k'_1 \neq k'} \mathbf{p}_{k,k'}(t) V_{k,k';k'_1,k_1}^{e,h}, \quad (9)$$

where $V_{k_1,k_2;k_3,k_4}^{\lambda,\lambda'}$ is the 1D Fourier transformed Coulomb potential between bands λ and λ' , i.e.

$$V_{k_1,k_2;k_3,k_4}^{\lambda,\lambda'} = \frac{e^2}{4\pi\epsilon_0\epsilon_b} \iint d^2r d^2r' \frac{[\Psi_{k_1}^\lambda(\mathbf{r})]^* [\Psi_{k_2}^{\lambda'}(\mathbf{r}')]^* \Psi_{k_3}^{\lambda'}(\mathbf{r}') \Psi_{k_4}^\lambda(\mathbf{r})}{|\mathbf{r} - \mathbf{r}'|} \quad (10)$$

Here, the electron and hole wave functions in a quantum wire are assumed to be $\Psi_k^{e,h}(\mathbf{r}) = \psi_0^{e,h}(x) \exp(iky) / \sqrt{\mathcal{L}}$. The functions $\psi_0^{e,h}(x) = (\alpha_{e,h} / \sqrt{\pi}) \exp(-\alpha_{e,h}^2 x^2 / 2)$ are the ground-state wavefunctions of electrons and holes in two transverse directions, where $\alpha_{e,h} = \sqrt{m_{e,h}^* \Omega_{e,h} / \hbar}$, $\hbar\Omega_{e,h}$ are the level separations between the ground and the first excited state of electrons and holes due to finite-size quantization, and α introduced in Eq. (6) is given by $2/\alpha = 1/\alpha_e + 1/\alpha_h$. With these assumptions, Eq. (10) becomes [29]

$$V_{k_1,k_2;k_3,k_4}^{\lambda,\lambda'} = \frac{e^2}{2\pi\epsilon_0\epsilon_b\mathcal{L}} \delta_{k_1+k_2-k_3-k_4} \iint dx dx' |\psi_0^\lambda(x)|^2 |\psi_0^{\lambda'}(x')|^2 K_0 \left(|k_4 - k_1| \sqrt{(x-x')^2 + \delta_0^2} \right). \quad (11)$$

2.3. Free-charge plasma response

The free-charge density in Eq. (1d) is calculated by

$$\tilde{\rho}_f(q, t) = \tilde{\rho}_h(q, t) + \tilde{\rho}_e(q, t). \quad (12)$$

In the limit of an infinitely long wire, the electron and hole densities are given by [27]

$$\tilde{\rho}_e(q, t) = -\frac{e\alpha}{\mathcal{L}\delta_0} \sum_k \langle \hat{\alpha}_{k-q}^\dagger \hat{\alpha}_k \rangle, \quad (13)$$

$$\tilde{\rho}_h(q, t) = +\frac{e\alpha}{\mathcal{L}\delta_0} \sum_{k'} \langle \hat{\beta}_{-(k'+q)}^\dagger \hat{\beta}_{-k'} \rangle, \quad (14)$$

where $\hat{\alpha}_k^\dagger$ and $\hat{\alpha}_k$ are the electron creation and annihilation operators, and $\hat{\beta}_k^\dagger$ and $\hat{\beta}_k$ are the hole creation and annihilation operators. However, as with the polarization in Eq. (6), to account for the borders of the quantum wire as given by the wire envelope function $g(y)$, we calculate the charge densities in the y -space of the wire as

$$\rho_e(y, t) = -\frac{e\alpha g(y)}{\mathcal{L}\delta_0} \sum_{k_1, k_2} \langle \hat{\alpha}_{k_1}^\dagger \hat{\alpha}_{k_2} \rangle e^{i(k_2 - k_1)y}, \quad (15)$$

$$\rho_h(y, t) = +\frac{e\alpha g(y)}{\mathcal{L}\delta_0} \sum_{k'_1, k'_2} \langle \hat{\beta}_{-k'_1}^\dagger \hat{\beta}_{-k'_2} \rangle e^{i(k'_1 - k'_2)y}. \quad (16)$$

The expectation values in Eqs. (15) and (16) require knowledge of the intraband carrier coherences, where the $k_1 \neq k_2$ and $k'_1 \neq k'_2$ terms provide for a non-uniform spatial distribution of the plasma. The plasma populations, where $k_1 = k_2$ and $k'_1 = k'_2$, are simply the occupation numbers $n_k^e = \langle \hat{\alpha}_k^\dagger \hat{\alpha}_k \rangle$ and $n_k^h = \langle \hat{\beta}_{-k}^\dagger \hat{\beta}_{-k} \rangle$ and are already calculated by Eqs. (5a) and (5b).

We account for the time-evolution of the electron intraband coherence by solving the equation

$$\frac{d}{dt} \langle \hat{\alpha}_{k_1}^\dagger \hat{\alpha}_{k_2} \rangle = \frac{i}{\hbar} \left[\hat{\mathcal{H}}_e + \hat{\mathcal{H}}_{\text{int}}, \hat{\alpha}_{k_1}^\dagger \hat{\alpha}_{k_2} \right], \quad (17)$$

where the single electron 1-band Hamiltonian $\hat{\mathcal{H}}_e$ is [27]

$$\hat{\mathcal{H}}_e = \sum_k \varepsilon_k^e \hat{\alpha}_k^\dagger \hat{\alpha}_k + \frac{1}{2} \sum_{k, k', q \neq 0} V_q \hat{\alpha}_{k-q}^\dagger \hat{\alpha}_{k'+q}^\dagger \hat{\alpha}_{k'} \hat{\alpha}_k. \quad (18)$$

Here, $V_q^{\text{ee}} = V_{k+q, k'-q, k', k}^{\text{ee}}$ is the Fourier transformed Coulomb potential given in Eq. (11), while ε_k^e is the carrier energy. The 2-band dipole interaction Hamiltonian $\hat{\mathcal{H}}_{\text{int}}$ is given by

$$\hat{\mathcal{H}}_{\text{int}} = - \sum_{k, k'} \left[d_{cv}^* \tilde{\mathcal{E}}^*(k - k', t) \hat{\beta}_{-k'} \hat{\alpha}_k + d_{cv} \tilde{\mathcal{E}}(k - k', t) \hat{\alpha}_k^\dagger \hat{\beta}_{-k'}^\dagger \right]. \quad (19)$$

For notational simplicity, we write the expectation value of the interband coherence operator as $P_{k, k'} = \langle \hat{\beta}_{-k'} \hat{\alpha}_k \rangle$. Adding these contributions into Eq. (17), the resulting equation for $k_1 \neq k_2$ intraband electron coherence is:

$$\begin{aligned} \frac{d}{dt} \langle \hat{\alpha}_{k_1}^\dagger \hat{\alpha}_{k_2} \rangle &= \frac{i}{\hbar} (\varepsilon_{k_1}^e - \varepsilon_{k_2}^e) \langle \hat{\alpha}_{k_1}^\dagger \hat{\alpha}_{k_2} \rangle + \frac{iV_{k_2 - k_1}^{\text{ee}}}{\hbar} (n_{k_2}^e - n_{k_1}^e) \sum_k \langle \hat{\alpha}_{k+k_1-k_2}^\dagger \hat{\alpha}_k \rangle \\ &+ \frac{i}{\hbar} \sum_{k'} \left[d_{cv} \tilde{\mathcal{E}}(k_2 - k', t) P_{k_1, k'}^* - d_{cv}^* \tilde{\mathcal{E}}^*(k_1 - k', t) P_{k_2, k'} \right]. \end{aligned} \quad (20)$$

Following the approach in Ref. [29], we let $P_{k, k'} \rightarrow \mathbf{p}_{k, k'}(t)$, and $d_{cv} \mathcal{E}_{k_2 - k'} P_{k_1, k'}^* \rightarrow d_{cv} \tilde{\mathbf{E}}(k_2 - k', t) \cdot \mathbf{p}_{k_1, k'}^*(t)$, to account for the multi-directional nature of the electric field and material response.

The final equation of motion for the intraband electron coherence is

$$\begin{aligned} \frac{d}{dt} \langle \hat{\alpha}_{k_1}^\dagger \hat{\alpha}_{k_2} \rangle &= \frac{i}{\hbar} (\varepsilon_{k_1}^e - \varepsilon_{k_2}^e) \langle \hat{\alpha}_{k_1}^\dagger \hat{\alpha}_{k_2} \rangle + \frac{iV_{k_2-k_1}^{vee}}{\hbar} (n_{k_2}^e - n_{k_1}^e) \sum_k \langle \hat{\alpha}_{k+k_1-k_2}^\dagger \hat{\alpha}_k \rangle \\ &+ \frac{i}{\hbar} \sum_{k'} \left[d_{cv} \tilde{\mathbf{E}}(k_2 - k', t) \cdot \mathbf{p}_{k_1, k'}^* (t) - d_{cv} \tilde{\mathbf{E}}^*(k_1 - k', t) \cdot \mathbf{p}_{k_2, k'} (t) \right]. \end{aligned} \quad (21)$$

An analogous calculation for the holes leads to:

$$\begin{aligned} \frac{d}{dt} \langle \hat{\beta}_{-k_1}^\dagger \hat{\beta}_{-k_2} \rangle &= \frac{i}{\hbar} (\varepsilon_{k_1}^h - \varepsilon_{k_2}^h) \langle \hat{\beta}_{-k_1}^\dagger \hat{\beta}_{-k_2} \rangle + \frac{iV_{k_2-k_1}^{hh}}{\hbar} (n_{k_2}^h - n_{k_1}^h) \sum_{k'} \langle \hat{\beta}_{-k'-k_1+k_2}^\dagger \hat{\beta}_{-k'} \rangle \\ &+ \frac{i}{\hbar} \sum_{k'} \left[d_{cv} \tilde{\mathbf{E}}(k - k_2', t) \cdot \mathbf{p}_{k, k_1'}^* (t) - d_{cv} \tilde{\mathbf{E}}^*(k - k_1', t) \cdot \mathbf{p}_{k, k_2'} (t) \right]. \end{aligned} \quad (22)$$

2.4. Dielectric functions

The longitudinal (plasma) dielectric susceptibility can be calculated by adding the contributions of electrons and holes,

$$\chi^\parallel(q, \omega) = \chi_e^\parallel(q, \omega) + \chi_h^\parallel(q, \omega), \quad (23)$$

where each contribution is given by a sum over states as

$$\chi_j^\parallel(q, \omega) = -\frac{V_{qj}^{jj}}{\pi} \int dk \frac{n_k^j - n_{k+q}^j}{\hbar\omega - \varepsilon_{k+q}^j + \varepsilon_k^j - i\hbar\gamma_j}, \quad (24)$$

and γ_j are the small electron and hole coherence decay rates. Note, the plasma frequency dispersion $\omega_p(q)$ can be obtained from the root of the equation $\Re[\varepsilon_j^\parallel(q, \omega)] = 1 + \Re[\chi_j^\parallel(q, \omega)] = 0$.

The transverse dielectric function $\varepsilon^\perp(q, \omega) = 1 + \chi^\perp(q, \omega)$ relates to the laser-induced interband transitions of electrons between the valence and conduction bands. By using the charge-current conservation law [33], it is calculated from the distributions after the pulse by:

$$\chi^\perp(q, \omega) = \frac{d_{cv}^2 \alpha}{2\epsilon_0 \epsilon_b \pi \delta_0} \int dk \left(\frac{1 - n_{k+q}^e - n_k^h}{\hbar\omega - \varepsilon_{k+q}^e - \varepsilon_k^h - \varepsilon_G - i\hbar\gamma_{eh}} \right), \quad (25)$$

where γ_{eh} is an approximate decay rate for electrons and holes.

3. Simulation description

As depicted in Fig. 1, the 1D laser pulse is linearly polarized in the x -direction with a peak field strength of 1.2 MV/cm, a pulsewidth of 40 fs, a central wavelength of 800 nm, and propagates along the y -axis. The quantum wire is 500 nm in length, lies along y -axis, and is centered about $y=0$. The width of the quantum wire is approximately 5 nm in the transverse directions (x and z directions). The wire itself is presumed to be pure GaAs embedded in an AlAs host medium ($\epsilon_b = 10.1$). We use a two-band model for the GaAs quantum wire with a band gap of 1.5 eV and effective electron/hole masses of $m_e^* = 0.07 m_0$ and $m_h^* = 0.45 m_0$.

Each simulation records the transverse laser and generated longitudinal electric fields as functions of space and time. Within the quantum wire, the simulations record the electron-hole distributions, coherence, and scattering rates as functions of crystal momentum k and time. They also record the laser generated quantum wire polarization and the laser-generated electron-hole free-charge density as functions of space and time.

4. Results

Figure 2(a) shows the transverse laser field in the wire, see Eq. (3), as a function of wire position and time that we obtain from solving the combined Maxwell equations and the SBEs. The tilting slope for the propagation of field maximum within a quantum wire measures the phase velocity of EM wave, and it reduces slightly due to renormalization by induced e-h plasmas. Figure 2(b) shows the corresponding transverse polarization we obtain using Eq. (6). The plots show that the laser pulse has completely passed through the quantum wire by $t = 350$ fs, and that the transverse bound charge response ends by this time. Figure 3 shows that the diagonal dephasing rates, which are responsible for the broadening of resonance in the induced interband coherence, also peak during this period but remain consistently around 1 THz^{-1} thereafter. Moreover, the diagonal dephasing rate of electrons is much larger than that of holes due to resonantly enhanced scattering of electrons by optical phonons.

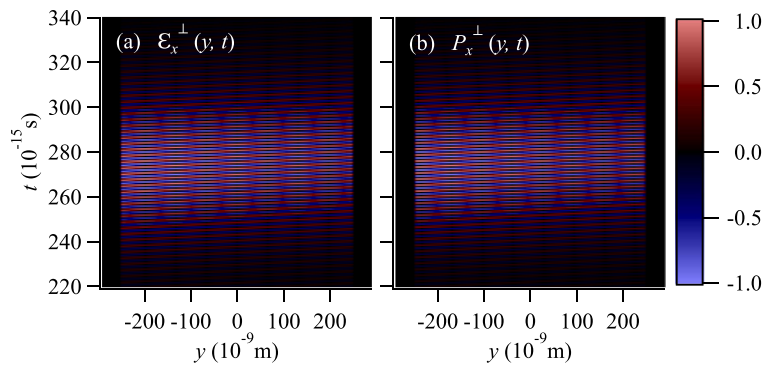


Fig. 2. The normalized (a) transverse electric field $\mathcal{E}_x^\perp(y, t)$ and (b) transverse quantum wire polarization field $P_x^\perp(y, t)$ as functions of wire position y and time t . The pump pulse peak occurs around 275 fs.

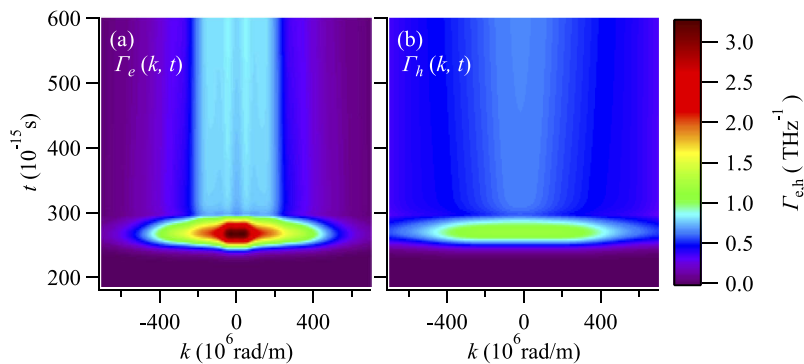


Fig. 3. The diagonal dephasing rates for (a) electrons $\Gamma_k^e(t)$ and (b) holes $\Gamma_k^h(t)$ as functions of momentum k and time t .

The transverse field in Fig. 2(a) excites electron-hole distributions, shown in Fig. 4 as functions of carrier momentum and time. Immediately after the initial excitation ($t > 350$ fs), the distributions have slightly off-center peaks, at higher energies above the gamma-point. After longer times ($t \gg 1$ ps), many-body effects (primarily carrier-phonon collisions) drive the initial non-equilibrium distributions to a quasi-equilibrium with a central peak within 10 ps. In addition, the side peaks in Fig. 4(a), which are associated with resonant scattering of electrons to the

gamma-point, decrease quickly with time after the central peak occurs. On the other hand, no side peaks and central peak are found for holes in Fig. 4(b), and a quasi-equilibrium state is reached much faster than that for electrons due largely to Coulomb scattering redistribution of carriers on this time-scale [34].

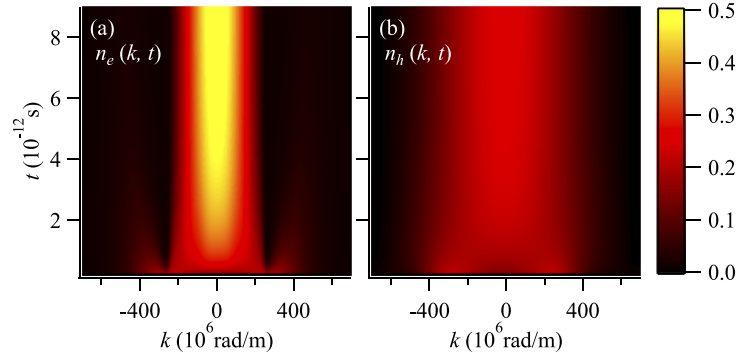


Fig. 4. The (a) electron distribution $n_k^e(t)$ and (b) the hole distribution $n_k^h(t)$ as functions of momentum k and time t after excitation from the pump pulse.

At all times, the carrier distributions excited in Fig. 4 are arranged non-uniformly along the wire as described by Eqs. (15) and (16) in Sec. 2.3. Figure 5(a) shows the generated net free-charge plasma density in the quantum wire as a function of wire position and time. We see that immediately following the pulse excitation, a spatially non-uniform plasma is created and plasma oscillations occur within the wire over time. The boundary between positive and negative charge regions is readily seen, and it switches with time initially as a standing wave but eventually collapses due to the large dissipation of induced intraband longitudinal plasmon modes in a quantum wire [1]. As per the Maxwell equations, we use the free charge density from Fig. 5(a) to calculate the longitudinal electric displacement $D_y^{\parallel}(y, t)$ shown in Fig. 5(b). If we treat the free-charge density like a bound-charge density, then we can formally define a free-charge polarization $P_f(y, t)$ according to the standard definition $\rho_f = -\vec{\nabla} \cdot \mathbf{P}_f$. Since we also require that $\rho_f = \vec{\nabla} \cdot \mathbf{D}$, it is clear that $P_f = -D_y^{\parallel}$ and Fig. 5(b) gives us the intraband longitudinal plasma polarization. The presence of a free-charge density in Fig. 5(a) creates a strong longitudinal electric field in the wire that oscillates as the standing-wave plasma oscillates. Figure 6 shows the interband longitudinal electric and polarization fields in the quantum wire as functions of wire position and time. The interband longitudinal bound-charge polarization, shown in Fig. 6(b), only slightly modifies the longitudinal electric field because the frequency of $E_y^{\parallel}(y, t)$, the plasma oscillation frequency, is well-below interband resonance in the wire. Additional simulation results shown in Fig. 7 confirm that these plasma oscillations do not occur without including the fully dynamical calculations of the intraband coherence terms as described in Eqs. (21) and (22). In the simulation for Fig. 7, the free-charge densities were estimated from the instantaneous values of the interband coherence $\mathbf{p}_{k,k'}(t)$ as found in [29]. This approximation neglects the back-action effects of the longitudinal electric field on the intraband coherence evolution as well as the plasma screening. Specifically, it is the first and third terms on the right-hand-sides of Eqs. (21) and (22) that are critical for capturing the intraband short-time plasma response. Meanwhile, the second term on the right-hand-sides of Eqs. (21) and (22) gives rise to long-time plasma screening and plays a smaller but non-negligible role in the plasma oscillations.

Figure 8 shows the real parts of the theoretical calculated susceptibilities as functions of q and ω after the trailing edge of the laser pulse has passed ($t = 3.5$ ps). Specifically, at this time Fig. 8(a) shows the calculation of $\Re[\chi^{-1}(q, \omega)]$ using Eq. (24), Fig. 8(b) shows the calculation

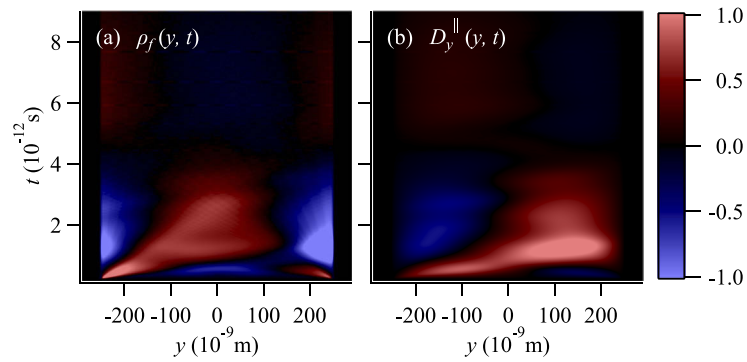


Fig. 5. The normalized (a) laser-generated free charge density $\rho_f(y, t)$ and (b) intraband longitudinal displacement field $D_y^{\parallel}(y, t)$ as functions of wire position y and time t .

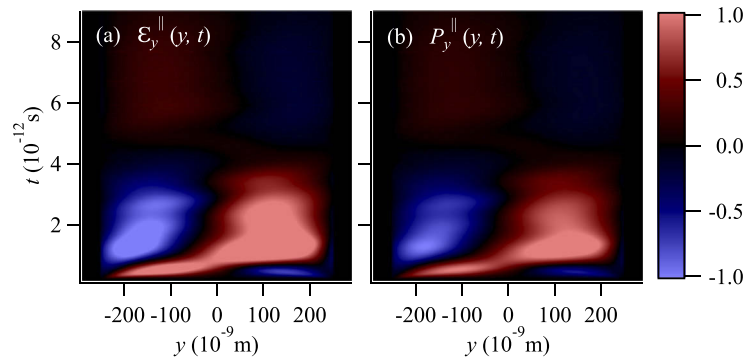


Fig. 6. The normalized (a) longitudinal electric field $\mathcal{E}_y^{\parallel}(y, t)$ and (b) interband longitudinal quantum wire polarization field $P_y^{\parallel}(y, t)$ as functions of wire position y and time t . The peak $\mathcal{E}_y^{\parallel}(y, t)$ value is approximately 4.7 MV/cm

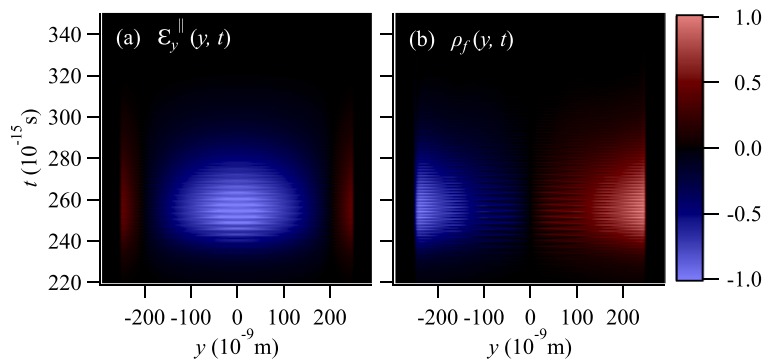


Fig. 7. The normalized (a) longitudinal electric field $\mathcal{E}_y^{\parallel}(y, t)$ and (b) laser-generated free charge density $\rho_f(y, t)$ as functions of wire position y and time t for calculations that do not solve Eqs. (21) and (22) for the intraband coherences, instead approximating the intraband coherence as shown in [29]. The peak $\mathcal{E}_y^{\parallel}(y, t)$ value is 0.25 MV/cm.

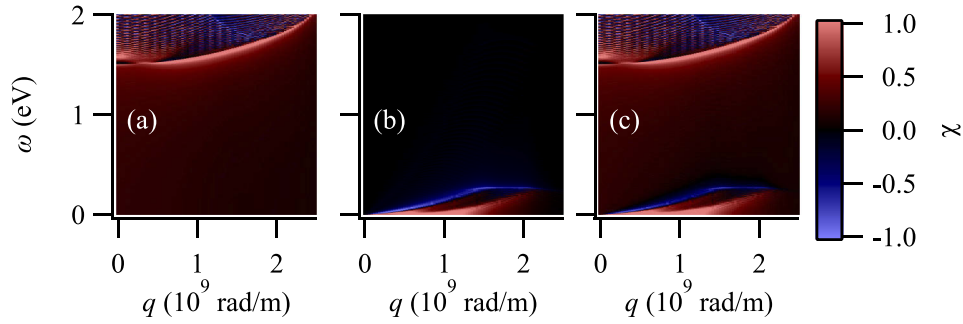


Fig. 8. The real parts of the quantum wire susceptibility for the (a) transverse and (b) longitudinal response. (c) The combined response.

of $\Re[\chi^{\parallel}(q, \omega)]$ using Eq. (23), and Fig. 8(c) shows these combined susceptibilities that any applied electric field would experience. Here, numerically computed occupation factors and energy dispersions at $t=3.5$ ps for electrons and holes have been utilized in evaluating Eqs (23) and (24). In Fig. 8(a), for frequencies below the band gap ($\omega < 1.5$ eV) we see a nearly constant positive value, decreasing gradually with increasing q while increasing with ω as one nears resonance. The resonance peak curve in $\Re[\chi^{\perp}(q, \omega)]$ moves upward in ω with increasing q because $q \neq 0$ represents a change in an electron's crystal momentum during a purely optical transition. The quadratic dependence on q indicates a renormalization of pulse-laser group velocity in a dielectric host by induced interband excitation of electrons within a quantum wire. For direct-gap semiconductors, such an interband $q \neq 0$ transition requires an energy resonance higher than the gamma-point band gap. Just above resonance, for many values of q , Fig. 8(a) shows that $\Re[\chi^{\perp}(q, \omega)]$ drops nearly to zero. This feature appears only after the pulse excitation and occurs because the electron and hole distributions are nearing peak values of 0.5 and 0.25, respectively, for times $t > 3$ ps (see Fig. 4), and also due to the broadened intraband resonance (see Fig. 3). Any applied electric field will experience the bound-charge interband dipole response shown in Fig. 8(a).

Figure 8(b) shows the purely longitudinal intraband plasma susceptibility $\Re[\chi^{\parallel}(q, \omega)]$ containing contributions from both the electron and hole plasmas. The below intraband-resonance values of $\chi^{\parallel}(q, \omega)$ are positive, while the appearance of the plasma resonance is clear as the blue negative curve in the low energy range, where $\Re[\chi^{\parallel}(q, \omega)] \leq -1$, and therefore $\Re[\epsilon^{\parallel}(q, \omega)] \leq 0$. Therefore, this contributes to the response that gives rise to the mode of plasma oscillations seen in Fig. 5 and Fig. 6(a). Figure 8(c) simply adds the susceptibilities of Fig. 8(a) and Fig. 8(b) together to show the combined interband and intraband response that an applied electric field will experience. In practice, an applied field will only detect the bound-charge interband response in Fig. 8(a) for optical fields, or the free-charge intraband response of Fig. 8(b) for THz fields. Here, the intraband excitations of electrons result from an internal longitudinal electric field due to net charge-density distribution within a quantum wire as a consequence of pulse-laser induced interband excitations of electrons. Such a localized THz field can be detected if a diffraction grating is deposited on a quantum wire structure so that this localized THz field can convert into a radiative one.

The simulation described in Sec. 3. was constructed to generate a significant e - h plasma ($n_{k \approx 0}^{e,h} \sim 10^{-1}$) using minimal pulse energy on the ultrafast time scale. We now comment on the robustness of this approach and its results. A modest increase in laser pulse energy or pulse width will increase number of excited carriers and may cause longer lasting and higher amplitude intraband plasma oscillations. However, a significant (a factor of 2 or more) increase in energy or pulse width may saturate the conduction band states near $k \approx 0$ and result in Rabi oscillations of

the e - h distributions. If one keeps the same pulse energy but with a longer (or shorter) ultrashort pulsewidth, it would change the spectral bandwidth and result in narrower (broader) absorption peaks in the electron-hole distributions during excitation. However, the results in Fig. 4 show that scattering events will relax these distributions within 10 ps, leaving the results qualitatively similar. If one alters the pulse frequency significantly then it will no longer be resonant with the wire and this paper's approach is no longer adequate. For off-resonance calculations, the entire band structure with multiple subbands must often be included for accuracy [5,35].

5. Conclusion

We couple a recent quantum-kinetic model for e - h plasma photo-generation and transport to the Maxwell equations and study the optoelectronic response of a semiconductor quantum wire excited by a resonant ultrashort laser pulse. In this model, the quantum-wire electrons interact with both propagating transverse and the generated longitudinal electric fields within the wire. By solving for both interband and intraband dynamical coherences, plasma oscillations emerge in the wire at THz frequencies. Furthermore, the back action of generated optical polarizations and e - h plasmas on transverse and longitudinal electric fields, as well as on the electrons themselves as a correlation effect, is included self-consistently. Due to the 1D nature of both the quantum wire and the propagation space, the transverse (optical) and longitudinal (plasmonic) fields and dielectric responses are easily distinguishable even when both are present in the same susceptibility component. Additional results show the e - h carrier dynamics (including Coulomb scattering and dephasing, as well as carrier-phonon scattering) cause the electron and hole distributions to reach different quasi-equilibrium states in less than 10 ps. This understanding of the electric transverse optical and longitudinal plasma responses in reduced dimensional solids is necessary for advances in the growing field of ultrafast optoelectronics. Specifically, our results allow for prediction of highly nonlinear optoelectronic behavior in novel nanoscale semiconductor devices.

Funding. National Science Foundation (PHY 1903462); Air Force Office of Scientific Research.

Acknowledgments. This work was supported in part by research computing resources and technical expertise via a partnership between Kennesaw State University's Office of the Vice President for Research and the Office of the CIO and Vice President for Information Technology [36].

Disclosures. The authors declare no conflicts of interest.

Data availability. Data underlying the results presented in this paper are not publicly available at this time but may be obtained from the authors upon reasonable request.

References

1. G. Gumbs and D. Huang, *Properties of Interacting Low-Dimensional Systems* (John Wiley & Sons, 2011).
2. A. Kaiser, B. Rethfeld, M. Vicanek, and G. Simon, "Microscopic processes in dielectrics under irradiation by subpicosecond laser pulses," *Phys. Rev. B* **61**(17), 11437–11450 (2000).
3. K. Wang and D. M. Mittleman, "Guided propagation of terahertz pulses on metal wires," *J. Opt. Soc. Am. B* **22**(9), 2001–2008 (2005).
4. P. González de Alaiza Martínez, X. Davoine, A. Debayle, L. Gremillet, and L. Bergé, "Terahertz radiation driven by two-color laser pulses at near-relativistic intensities: Competition between photoionization and wakefield effects," *Sci. Rep.* **6**(1), 26743 (2016).
5. O. Schubert, M. Hohenleutner, F. Langer, B. Urbanek, C. Lange, U. Huttner, D. Golde, T. Meier, M. Kira, S. W. Koch, and R. Huber, "Sub-cycle control of terahertz high-harmonic generation by dynamical Bloch oscillations," *Nat. Photonics* **8**(2), 119–123 (2014).
6. D. Huang, G. Gumbs, P. M. Alsing, and D. A. Cardimona, "Nonlocal mode mixing and surface-plasmon-polariton-mediated enhancement of diffracted terahertz fields by a conductive grating," *Phys. Rev. B* **77**(16), 165404 (2008).
7. D. Huang and M. O. Manasreh, "Intersubband transitions in strained $\text{In}_{0.07}\text{Ga}_{0.93}\text{As}/\text{Al}_{0.40}\text{Ga}_{0.60}\text{As}$ multiple quantum wells and their application to a two-colors photodetector," *Phys. Rev. B* **54**(8), 5620–5628 (1996).
8. F. Krausz and M. I. Stockman, "Attosecond metrology: from electron capture to future signal processing," *Nat. Photonics* **8**(3), 205–213 (2014).

9. A. Schiffrin, T. Paasch-Colberg, N. Karpowicz, V. Apalkov, D. Gerster, S. Mühlbrandt, M. Korbman, J. Reichert, M. Schultze, S. Holzner, J. V. Barth, R. Kienberger, R. Ernstorfer, V. S. Yakovlev, M. I. Stockman, and F. Krausz, "Optical-field-induced current in dielectrics," *Nature* **493**(7430), 70–74 (2012).
10. G. Vampa, T. J. Hammond, M. Taucer, X. Ding, X. Ropagnol, T. Ozaki, S. Delprat, M. Chaker, N. Thiré, B. E. Schmidt, F. Légaré, D. D. Klug, A. Y. Naumov, D. M. Villeneuve, A. Staudte, and P. B. Corkum, "Strong-field optoelectronics in solids," *Nat. Photonics* **12**(8), 465–468 (2018).
11. G. Vampa and T. Brabec, "Merge of high harmonic generation from gases and solids and its implications for attosecond science," *J. Phys. B* **50**(8), 083001 (2017).
12. F. Krausz, "The birth of attosecond physics and its coming of age," *Phys. Scr.* **91**(6), 063011 (2016).
13. S. Ghimire, G. Ndabashimiye, A. D. DiChiara, E. Sistrunk, M. I. Stockman, P. Agostini, L. F. DiMauro, and D. A. Reis, "Strong-field and attosecond physics in solids," *J. of Phys. B* **47**(20), 204030 (2014).
14. A. Sommer, E. M. Bothschafter, S. A. Sato, C. Jakubeit, T. Latka, O. Razskazovskaya, H. Fattahi, M. Jobst, W. Schweinberger, V. Shirvanyan, V. S. Yakovlev, R. Kienberger, K. Yabana, N. Karpowicz, M. Schultze, and F. Krausz, "Attosecond nonlinear polarization and light–matter energy transfer in solids," *Nature* **534**(7605), 86–90 (2016).
15. G. Orlando, C.-M. Wang, T.-S. Ho, and S.-I. Chu, "High-order harmonic generation in disordered semiconductors," *J. Opt. Soc. Am. B* **35**(4), 680–688 (2018).
16. D. Huang, T. Apostolova, P. M. Alsing, and D. A. Cardimona, "High-field transport of electrons and radiative effects using coupled force-balance and fokker-planck equations beyond the relaxation-time approximation," *Phys. Rev. B* **69**(7), 075214 (2004).
17. S. Mokkaapati and C. Jagadish, "Review on photonic properties of nanowires for photovoltaics," *Opt. Express* **24**(15), 17345–17358 (2016).
18. X. Wang, M. R. Khan, M. Lundstrom, and P. Bermel, "Performance-limiting factors for gaas-based single nanowire photovoltaics," *Opt. Express* **22**(S2), A344–A358 (2014).
19. K. F. MacDonald, Z. L. Sámson, M. I. Stockman, and N. I. Zheludev, "Ultrafast active plasmonics," *Nat. Photonics* **3**(1), 55–58 (2008).
20. M. I. Stockman, "Nanoplasmonics: The physics behind the applications," *Phys. Today* **64**(2), 39–44 (2011).
21. A. Iurov, G. Gumbs, D. Huang, and G. Balakrishnan, "Thermal plasmons controlled by different thermal-convolution paths in tunable extrinsic dirac structures," *Phys. Rev. B* **96**(24), 245403 (2017).
22. A. I. Lvovsky, B. C. Sanders, and W. Tittel, "Optical quantum memory," *Nat. Photonics* **3**(12), 706–714 (2009).
23. Y. R. Shen, *The Principles of Nonlinear Optics* (John Wiley and Sons, Inc., 1984).
24. S. Mukamel, *Principles of Nonlinear Optical Spectroscopy* (Oxford University, 1995).
25. M. Malinauskas, A. Žukauskas, S. Hasegawa, Y. Hayasaki, V. Mizeikis, R. Buividas, and S. Juodkazis, "Ultrafast laser processing of materials: from science to industry," *Light: Science & Applications* **5**(8), e16133 (2016).
26. M. Beresna, M. Gecevičius, and P. G. Kazansky, "Ultrafast laser direct writing and nanostructuring in transparent materials," *Adv. Opt. Photon.* **6**(3), 293–339 (2014).
27. H. Haug and S. W. Koch, *Quantum Theory of the Optical and Electronic Properties of Semiconductors* (World Scientific Publishing Co. Pte. Ltd., 2009), 5th ed.
28. J.-C. Diels and W. Rudolf, *Ultrashort Laser Pulse Phenomenon: Fundamentals, Techniques, and Applications on a Femtosecond Time Scale* (Academic, 2006), 2nd ed.
29. J. R. Gulley and D. Huang, "Self-consistent quantum-kinetic theory for interplay between pulsed-laser excitation and nonlinear carrier transport in a quantum-wire array," *Opt. Express* **27**(12), 17154–17185 (2019).
30. A. Taflove and S. C. Hagness, *Computational Electrodynamics: The Finite-Difference Time-Domain Method* (Artech House, Inc., 2000), 3rd ed.
31. E. O. Kane, "Band structure of indium antimonide," *J. Phys. Chem. Solids* **1**(4), 249–261 (1957).
32. U. Bockelmann and G. Bastard, "Interband absorption in quantum wires. i. zero-magnetic-field case," *Phys. Rev. B* **45**(4), 1688–1699 (1992).
33. F. Forstmann and R. R. Gerhardt, *Metal optics near the plasma frequency* (Springer-Verlag New York Inc, United States, 1986).
34. K. Huthmacher, A. K. Molberg, B. Rethfeld, and J. R. Gulley, "A split-step method to include electron–electron collisions via monte carlo in multiple rate equation simulations," *J. Comput. Phys.* **322**, 535–546 (2016).
35. I. Kilen, M. Kolesik, J. Hader, J. V. Moloney, U. Huttner, M. K. Hagen, and S. W. Koch, "Propagation induced dephasing in semiconductor high-harmonic generation," *Phys. Rev. Lett.* **125**(8), 083901 (2020).
36. T. Boyle and R. Aygun, "High performance computing system," Tech. rep., Kennesaw State University (2021).